Journal of Applied Fluid Mechanics, Vol. 18, No. 1, pp. 260-273, 2025.
Available online at www.jafmonline.net, ISSN 1735-3572, EISSN 1735-3645.
https://doi.org/10.47176/jafm.18.1.2687

Numerical Study of the Effect of Rail Modelling Method on Train Aerodynamic Performance and Slipstream

Y. Ma, J. Zhang†, J. Shi and Y. Cao

State Key Laboratory of Rail Transit Vehicle System, Southwest Jiaotong University, Chengdu, Sichuan Province, 610031, China

†Corresponding Author Email: jyzhang@swjtu.edu.cn

ABSTRACT

The high-speed movement of trains generates train-induced wind, commonly referred to as slipstream, which presents a specific safety concern for passengers and personnel. Yet, the fastening system employed to secure ballastless tracks, characterised by its complex shape, substantial quantity, and dense arrangement, remains inadequately investigated regarding its influence on train aerodynamics. In the present study, a sliding mesh technique was employed to comparatively examine the impact of different track configurations—trackless, track-only, and track with a fastening system—on the aerodynamic characteristics, slipstream formation, and wake turbulence induced by trains. The results indicate that the tracks and the fastening system increased the drag force coefficient by 0.73% and 2.05%, respectively, compared with no track. Additionally, tracks and the fastening system had a significant impact on the slipstream velocity near the train and ground. Tracks notably altered the shape of the wake near the ground, and the fastening system exacerbated this phenomenon. Further, the fastening system further intensified the generation of secondary vortices at track and footstep locations.

Article History

Received February 28, 2024
Revised July 12, 2024
Accepted July 26, 2024
Available online November 6, 2024

Keywords:

High-speed train
Slipstream
Track
Fastening system
Aerodynamic
Wake

1. INTRODUCTION

Since the introduction of high-speed trains in the last century, they have been widely adopted for their efficiency, environmental benefits, and other advantages, progressively becoming the dominant mode of ground transportation. During the preceding century, Japan's Shinkansen and Germany's ICE high-speed trains underwent rapid development (Raghunathan et al., 2002). From the beginning of the new century, China has incorporated technology from Germany and Japan to embark on the development of its own high-speed trains, exemplified by models such as the Hexie (CRH) and Fuxing (CR). China's high-speed railways, such as those on the Beijing-Shanghai High-Speed Railway, can achieve a maximum speed of 350 km/h. As people pursue higher speeds, there should be a growing focus on the aerodynamics of trains (Tian, 2019).

Most researchers concentrate their efforts on studying areas such as increasing train speeds, diagnosing bogie faults, wheel-rail wear, and track conditions. As train speeds continue to rise and advancements occur in other fields, there is an increasing awareness and research interest in train aerodynamics. It is crucial to investigate the mechanisms and developmental processes of slipstream. In response, the European Committee for Standardisation (CEN) has enacted regulations to restrict the maximum slipstream speed of trains (CEN, 2009, 2010, 2013). Through observation of the flow field structure around high-speed trains, it has been observed that the interaction of head-nose pressure, train wake flow, airflow within the bogies, and the boundary layer development collectively contribute to the formation of the slipstream of high-speed trains (Baker, 2010). Factors influencing the high-speed train slipstream include not only the shape of the train head and its length-to-width-to-height ratio but also the surrounding facilities (Cheli et al., 2010; Bell et al., 2014) and natural conditions (Jönsson et al., 2014). Wang systematically compared the wake of two geometric configurations, trackless and tracked, analysing the impact of the track on the slipstream characteristics of high-speed trains and revealing the potential mechanisms by which the track shapes the wake structure (Wang et al., 2020). Bell's team (Bell et al., 2015) identified the detachment of a twin tail vortex separates from the rear of the train, which gradually develop towards the ground over time. Even small-sized tracks have a certain influence on the formation and development of the train's wake. Wang's study (Wang et al., 2018), which focused on the flow structure, slipstream characteristics, and aerodynamic properties of train models without bogies and with simplified

NOMENCLATURE

Symbols		***Greek***	
A	area of positive projection	ω	vorticity
u	velocity	ρ	density
Cp	pressure coefficient	***Abbreviations***	
Cd	drag force coefficient	*NR*	No Rail
Cl	lift force coefficient	*WR*	With Rail
		WRFS	With Rail Fastening System

bogies, revealed the influence of the bogie on the slipstream and wake of the train. Paz et al. (2017), using a sliding mesh approach and considering the shape of sleepers, observed that the train's drag coefficient increased by 15%, and the presence of sleepers favoured ballast projection. In Wang's research (Wang et al., 2020), the performance of three extensively used models in predicting the slipstream of full-scale train models was investigated. The three models included URANS, SAS, and DES. This assessment aims to identify the suitability of different turbulence modelling approaches to simulate aspects of slipstreams. Additionally, several scholars have conducted field experiments on train slipstream. Soper (Soper et al., 2017) measured the underside flow characteristics and track conditions of high-speed trains on a railway in Southern England. It was found that on well-maintained tracks, the magnitudes of mechanical forces and aerodynamics related to track displacement were similar. However, for tracks with higher acceleration and poor maintenance, the impact of track vibrations on ballast movement may be much more significant.

However, traditional methods assume the train is stationary and set a specified velocity at the inlet to simulate wind blowing over the train, akin to a wind tunnel. This approach exhibits certain disparities with real-world scenarios. The use of sliding mesh effectively bridges this gap, providing a better simulation of the interaction among moving trains, air, and ground facilities. Niu et al. (2021) analysed and compared the aerodynamics of stationary and moving trains, as well as the flow field beneath the train. In research areas such as trains passing through tunnels (Wang et al., 2022) and encounters between two trains (Chu et al., 2014; Sun et al., 2014), sliding mesh technology is extensively applied. Additionally, in Wang's study (Wang et al., 2023) on snow accumulation in the bogie region, a comparison between sliding mesh and non-sliding mesh conditions was conducted. The study validated its findings through wind tunnel experiments, showing that moving trains accumulate more snow in the bogie area. In conclusion, sliding mesh technology has proven effective in capturing the flow field structure beneath trains and simulating train slipstream more accurately.

Existing high-speed trains mostly utilise ballastless tracks, devoid of gravel and sleepers. The track is secured to reinforced concrete ground through a fastening system. The fastening system has a complex structure, with a large and dense quantity. Currently, there is a lack of research on the impact of the fastening system on the aerodynamic performance of high-speed trains, the flow field structure around bogies, and the formation of train slipstream.

In the present study, sliding mesh technology was adopted. Further, based on a 3-car model of a high-speed train, ground models were established: no rail ground (NR), with-rail ground (WR), and with-rail-fastening-system ground (WRFS). The drag and lift coefficients of the train, the flow field structure of the bogies, slipstream velocity surrounding the train, and the train's wake flow were all compared and analysed. Based on the present findings, recommendations are offered for choosing a track model in future numerical studies.

The paper is structured as the following. Section 2 presents the calculation model, meshing strategy, numerical methods and validation. Section 3 compares and analyses the train aerodynamics.

2. NUMERICAL MODELLING, METHODOLOGY AND VALIDATION

2.1 Train Geometry

In the numerical study, a 1:1 scale model of the CRH380B high-speed train was selected. The train consisted of a head car, a middle car, and a tail car. The dimensions of the train were 3.884 m in height, 3.255 m in width, and 76.72 m in length. The bogie structure was essentially complete, including components such as brake pads, swing arms, primary and secondary suspensions, anti-roll bars, lateral dampers, and traction rods, as shown in Fig. 1.

2.2 Railway Fastening System

A model of the railway fastening system was built based on the type 300 fastening system (a type of fastening), which can be effectively adjusted to the rail

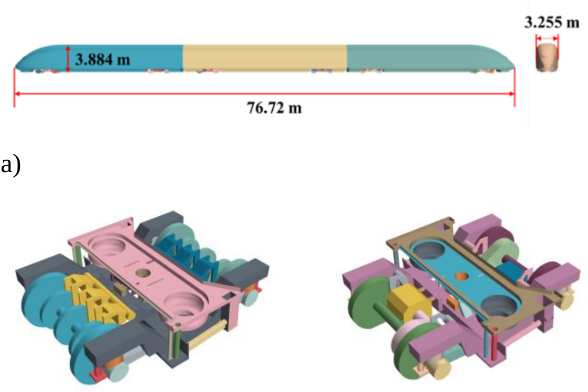

(a)

(b) (c)

Fig. 1 (a) Train geometrical model; (b) Trailing bogie; and (c) Motor bogie

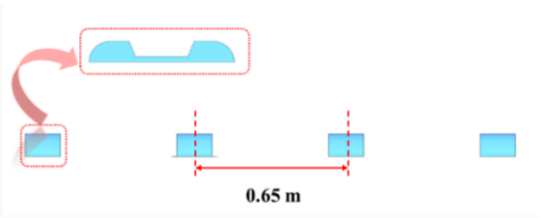

Fig. 2 Railway fastening system

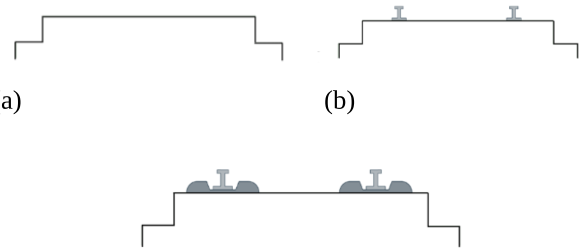
(a)
(b)
(c)

Fig. 3 Comparison cases: (a) NR; (b) WR; and (c) WRFS

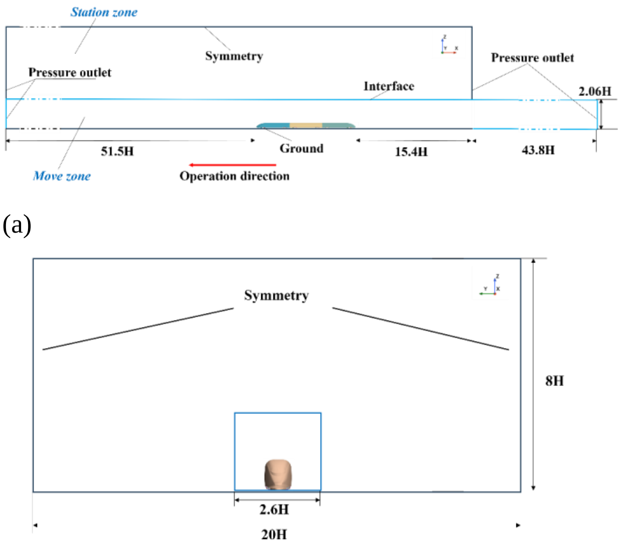

(a)

(b)

Fig. 4 Computational domain: (a) Side view; and (b) Front view

height by adding shims, as shown in Fig. 2. The spacing between two fasteners was 0.65 m. Figure 3 shows the NR, WR and WRFS models, respectively.

2.3 Boundary Conditions and Computational Domain

In the present study, a more realistic sliding mesh technology was adopted as the basis for establishing the computational domain, as illustrated in Fig. 4. The size of the domain was kept consistent across simulation cases. The domain was divided into a stationary zone and a moving zone containing the train. The inlet was positioned 200 m from the train's nose, and the outlet in the stationary zone was 60 m from the train's tail. The entrances to the stationary and moving areas were in the same plane, with a non-overlapping length of 170 m between the two regions.

All inlets and outlets of the computational domain are established as pressure outlets, the ground and track were treated as stationary walls, and the overlapping area of the stationary and moving zones was defined as interfaces. The top and sides were set as symmetric walls. Considering the operational speed range of the CRH380B train in China, a train speed of 250 km/h was set for the simulations, meaning that the moving zone advanced forward at 69.44m/s.

2.4 Computational Method

Based on previous research, the Reynolds-Averaged Navier-Stokes (RANS) equations are widely utilized to investigate the aerodynamic characteristics of high-speed trains. The RANS model has undergone extensive research and validation, incorporating a variety of mature turbulence models, particularly in engineering applications. Compared to direct numerical simulation (DNS) and large eddy simulation (LES), the RANS model reduces computational demands by averaging turbulent features in the flow field, thus focusing on larger-scale turbulent structures. This implies its capability to handle larger problem spaces in a shorter time. Of greater significance, the *k-epsilon* model provides more accurate predictions for flows away from the wall, which is a focal point of the present study.

As such, the three-dimensional unsteady incompressible Navier-Stokes equations and the realizable *k-epsilon* turbulence model were employed in the present study. The SIMPLEC algorithm was used to solve the pressure-velocity coupled equations, and a second-order discretisation was applied to all variables (Fluent Inc, 2015).

The Reynolds-averaged Navier-Stokes equations are as below:

$$\frac{\partial\rho}{\partial t}+\frac{\partial}{\partial x_i}(\rho u_i)=0 \tag{1}$$

$$\frac{\partial}{\partial t}(\rho u_i)+\frac{\partial}{\partial x_j}(\rho u_i u_j)=-\frac{\partial p}{\partial x_i}$$
$$+\frac{\partial}{\partial x_j}\left[\mu\left(\frac{\partial u_i}{\partial x_j}+\frac{\partial u_j}{\partial x_i}-\frac{2}{3}\delta_{ij}\frac{\partial u_i}{\partial x_i}\right)\right]+\frac{\partial}{\partial x_j}\left(-\rho\overline{u_i{}' u_j{}'}\right) \tag{2}$$

where u_i and u_j are the velocity components; x_i and x_j are the coordinate components; and ρ is the density of the liquid.

The simulated transport equations in the realizable *k-epsilon* turbulence model are:

$$\frac{\partial}{\partial t}(\rho k)+\frac{\partial}{\partial x_j}(\rho k u_j)=\frac{\partial}{\partial x_j}\left[\left(\mu+\frac{\mu_t}{\sigma_k}\right)\frac{\partial k}{\partial x_j}\right]$$
$$+G_k+G_b-\rho\varepsilon-Y_M+S_k \tag{3}$$

$$\frac{\partial}{\partial t}(\rho\varepsilon)+\frac{\partial}{\partial x_j}[\rho\varepsilon u_j]=\frac{\partial}{\partial x_j}\left[\left(\mu+\frac{\mu_t}{\sigma_\varepsilon}\right)\frac{\partial\varepsilon}{\partial x_j}\right]$$
$$+\rho C_1 S\varepsilon-\rho C_2\frac{\varepsilon^2}{k+\sqrt{v\varepsilon}}+C_{1\varepsilon}\frac{\varepsilon}{k}C_{3\varepsilon}G_b+S_\varepsilon \tag{4}$$

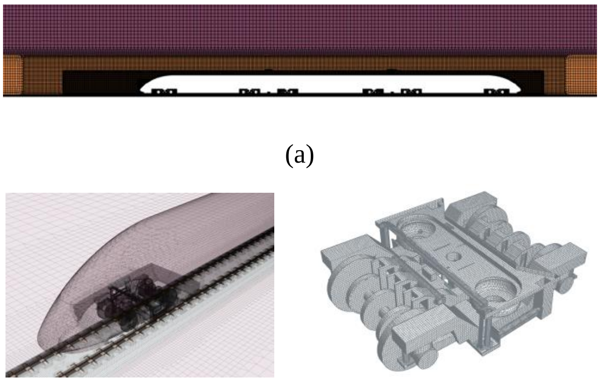

(a)

(b) (c)

Fig. 5 Computational grid: (a) Refinement boxes, (b) Surface mesh of train body and (c) Surface mesh of bogie

$$C_1 = max\left[0.43, \frac{\eta}{\eta+5}\right], \eta = S\frac{k}{\varepsilon}, S = \sqrt{2S_{ij}S_{ij}} \qquad (5)$$

In the equations, G_k denotes the turbulent kinetic energy produced by the mean velocity gradient; G_b means the turbulent kinetic energy produced by the buoyancy force; Y_M indicates the contribution of fluctuating dilatancy to the total dissipation rate in compressible turbulence; C_2 and $C_{1\varepsilon}$ are constants; S_k and S_ε are the turbulent Prandtl numbers for k and ε, respectively; S_k and S_ε represent user-defined source terms.

The time step for the simulations in the present study was set to 0.0005s. The flow field reached a basic stability within the first 0-0.5s of the simulation time. Time-averaging of the flow field results began from 0.5s and continued for 2.2s. The total simulation time was 2.7s.

2.5 Grid strategy and Grid Independence

Two refinements were placed around the train, and six refinements were also placed around each bogie. To enhance the accuracy of capturing the flow around the track, the surface grid size of the track and fastening system was set relatively small. Boundary layers were introduced on all surfaces of the train, ground, and track. The first layer thickness was 0.5 mm, and the grid growth rate was set to 1.2. In all cases, 12 boundary layers were included to maintain a y+ within the reasonable range of 30-300. Figure 5 shows the details of the grid.

In order to eliminate the effects of the grid, three sets of grids with different sizes were discretised for the CRH380B train. All the refinements were the same for different cases. Table 1 shows the comparison of drag coefficients of the head, middle and tail cars with different numbers of grids. The deviation in the total train drag coefficients was 0.44% for coarse and fine grids, and 0.07% for medium and fine grids. Figure 6 illustrates the pressure coefficients on the train surface along the centreline for different numbers of grids. The pressure coefficients of the fine and medium grids showed exceptional agreement for both the head and tail of the train. However, some deviation was observed between the coarse and fine grids, particularly noticeable in locally enlarged views. The grid sensitivity test indicates that the medium grid was adequate for the calculations. Based on the aforementioned settings, the numbers of grids for the NR, WR, and WRFS models were 51 million, 61 million, and 87 million, respectively.

Table 1 Aerodynamic drag force coefficients obtained using different grids

Aerodynamic drag force coefficient	Coarse	Medium	Fine
Mesh number millions	36.10	51.66	71.60
Head	0.1194	0.1200	0.1201
Middle	0.0663	0.0665	0.0659
Tail	0.0883	0.0865	0.0868
Total	0.2740	0.2730	0.2728

2.6 Numerical Validation

2.6.1 Pressure Coefficient Validation

The train centreline pressure coefficients obtained in the present study were compared with wind tunnel tests conducted in a 6.5m (width), 4.25m (height), and 15m (length) wind tunnel at the Shanghai Automotive Wind Tunnel Center (Xia et al., 2017). The maximum wind speed of the wind tunnel was 250 km/h. The test model had the same geometry, and the test field was a stationary ground. The comparison of pressure coefficient (Cp) between simulation and wind tunnel test is shown in Fig. 6. Evidently, there was a good agreement between the CFD results and the experiment results.

$$Cp = \frac{P-P_\infty}{0.5\rho u_{train}^2} \qquad (6)$$

where Cp is the dimensionless pressure coefficient; P is the surface pressure; P_∞ is the reference pressure; ρ is the air density; and U_{train} is the train running speed.

2.6.2 Slipstream Validation

Experiments on slipstream caused by high-speed trains were conducted using a moving model technique. Data measured at monitoring points were converted from the time domain to the spatial domain to determine slipstream velocities at specific locations adjacent to the train. The experiment utilised the ICE3 model, a high-speed train operating in Germany. The CRH380B train explored in the present study is an improved version based on the ICE3, sharing the same exterior design.

To validate the effectiveness of numerical methods in predicting turbulence at the bottom of a train, numerical results of slipstream velocity at the train's underside were compared with wind tunnel experiments. Slipstream velocity refers to the synthesised value of the streamwise direction velocity and the spanwise direction velocity. Vertical velocity was not considered because it does not pose a potential hazard to a standing person. Slipstream velocity is regarded as dimensionless in Eq. (11). The European Railway Agency proposes two typical slipstream measurement locations—one at 3m from the centreline of the track and 0.2m above the track surface, and the other at 3m from the centreline and 1.58m above

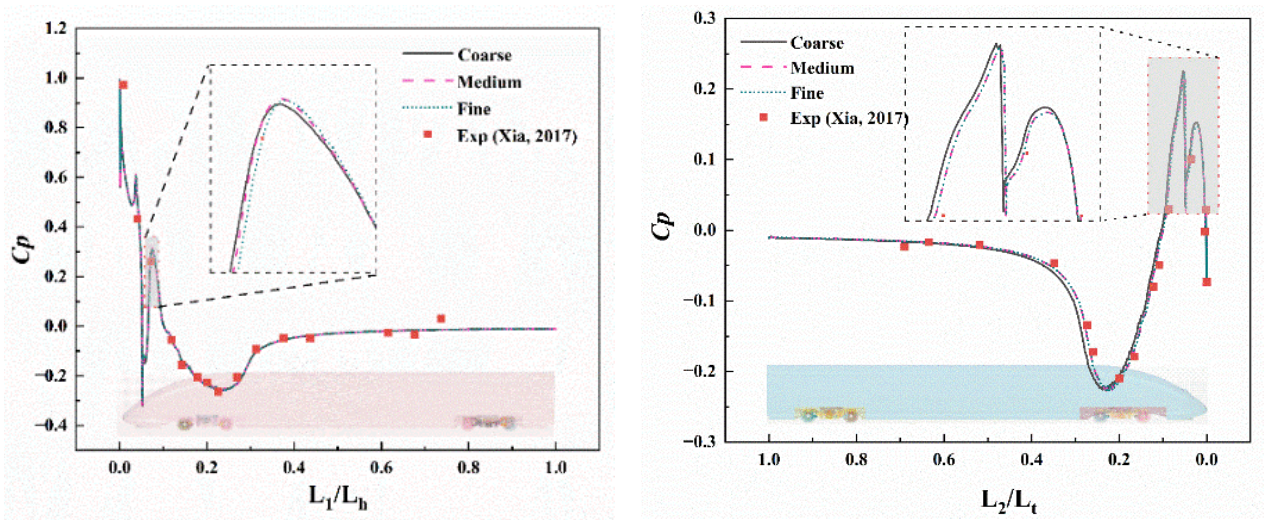

(a) (b)

Fig. 6 Pressure Coefficient Comparison (Cp) for the coarse, medium, and fine grids, as well as the experiment: (a) Head car; and (b) Tail car. (L1: distance to the train head, LH: overall length of the head; L2: distance to the tail of the train, LH: overall tail length)

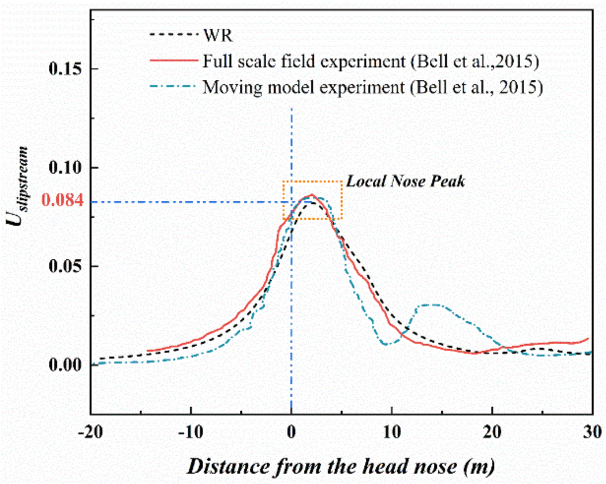

Fig. 7 Comparison of slipstream velocity at the monitor position

the track surface, corresponding to the height of railway station platforms. In the present study, the first measurement point was selected. The simulated slipstream velocity was compared with experimental data (Bell et al., 2015), as shown in Fig. 7.

$$U_{slipstream} = \frac{\sqrt{u_x^2+u_y^2}}{u_{train}} \tag{7}$$

where $U_{slipstream}$ is the slipstream velocity; u_x is the streamwise velocity; u_y is the spanwise velocity; and U_{train} is the train running speed.

As seen from Fig. 7, the present results exhibit a similar developmental trend to the experimental results. The sliding mesh technique used in the present study could capture the slipstream peak appearing at the head of the train well. The deviation of the peak from the moving model experiments was 2.38%, and the deviation from the full-scale model experimental results was 2.80%. The agreement between the simulation results and the experimental results shows that the numerical method used in the present study can predict the slipstream velocity around the train relatively accurately.

3. NUMERICAL RESULTS

This section is divided into three subsections. The first part provides a comparison of the aerodynamic performance of trains; the second part gives a description of the slipstream velocity of the train; and the third part includes an assessment of the wake flow.

To better compare the flow field changes caused by the slipstream around the train, several monitoring points were strategically placed in front of the train to measure various physical quantities for subsequent analysis, as shown in Fig. 8. The monitoring points were sequentially named M1-M11. After the calculations were completed, the results obtained in the time domain were transformed into the spatial domain. This process involved capturing the flow field conditions from 20m in front of the train's locomotive to 56m behind it.

3.1 Aerodynamic Force

Tables 2 and 3 respectively present the comparisons of drag force coefficient (C_d) and lift force coefficient (C_l) for the head, middle and tail cars of the train for different track types, respectively. The total drag coefficients were 0.2730, 0.2750 and 0.2786, respectively. There was an increase of 0.73% in WR drag coefficient and 2.05% in WRFS drag coefficient compared to NR. The total lift coefficients were 0.0124, 0.0153 and 0.0142, respectively.

$$C_d = \frac{F_d}{0.5\rho A u_{train}^2} \tag{8}$$

$$C_l = \frac{F_l}{0.5\rho A u_{train}^2} \tag{9}$$

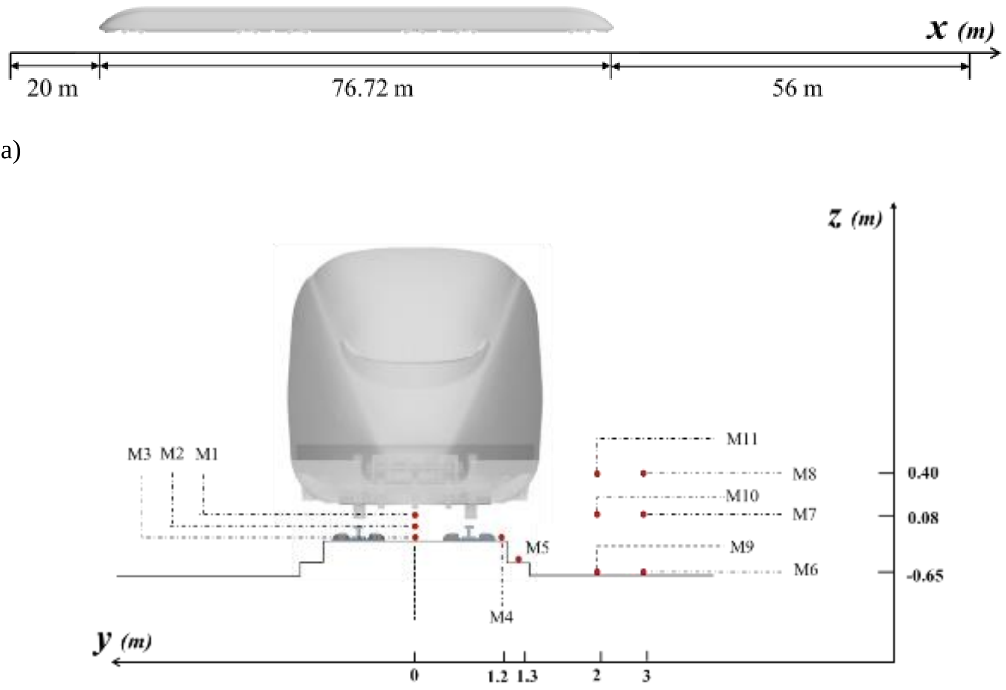

(a)

(b)

Fig. 8 Schematic location of monitoring: (a) Range of monitoring distances; (b) Specific location of monitoring points in the plane

Table 2 Comparison of aerodynamic drag force coefficient

	NR	WR	WRFS
Head	0.1200	0.1147	0.1136
Middle	0.0665	0.0674	0.0689
Tail	0.0865	0.0930	0.0961
Total	0.2730	0.2750	0.2786

Table 3 Comparison of aerodynamic lift force coefficient

	NR	WR	WRFS
Head	-0.0511	-0.0505	-0.0500
Middle	0.0001	0.0016	0.0012
Tail	0.0634	0.0642	0.0630

where F_d is drag force; F_l is lift force; ρ is density of air; and A is area of positive projection in the direction of train travel.

Evidently, only the drag coefficient of the head car decreased, while the drag coefficients of the middle car and tail car both increased. Conversely, in terms of lift coefficients, NR was the smallest, followed by WRFS, and WR exhibited the highest value. Figure 9 illustrates the contour of pressure coefficient at the bottom of the head car. The negative pressure at the bottom decreased from NR to WR to WRFS. The airflow typically entered the bogie from the rear wheels and then continued to travel forward. The presence of the track and the fastening system disturbed the airflow at the bottom of the train and reduced the slipstream caused by the high-speed movement of the train, as shown in Fig. 10. Moreover, the reduction of the air flow velocity on the ground and near the track also led to a significant reduction of the negative pressure on the ground, as shown in Fig. 11. In WR, the track had a certain sealing effect on the internal air, leading to the accumulation and compression of internal air, thereby generating a certain upward force on the train. This accounted for the increased lift force. For WRFS, there were significant gaps between the track fastening system and the ground, resulting in a reduced hindrance to the airflow by the track. This explains why the lift of WRFS falls between that of NR and WR configurations.

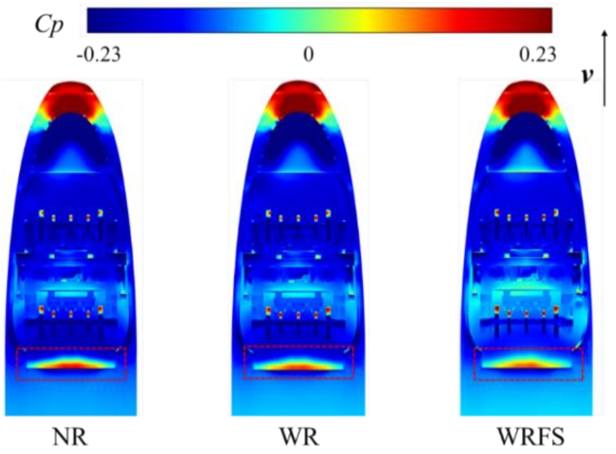

Fig. 9 Time averaged pressure contours on the bottom of the head car

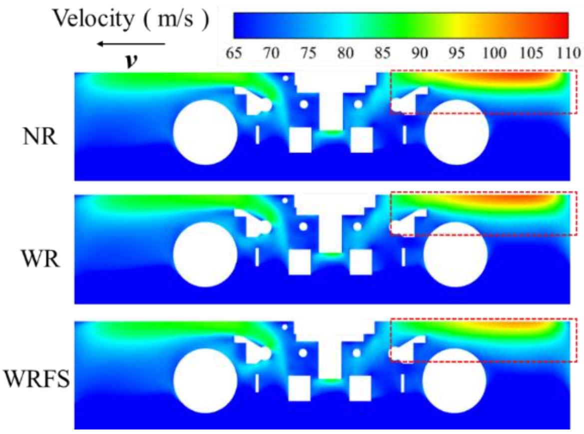

Fig. 10 Time averaged velocity contours on longitudinal central section of the first bogie

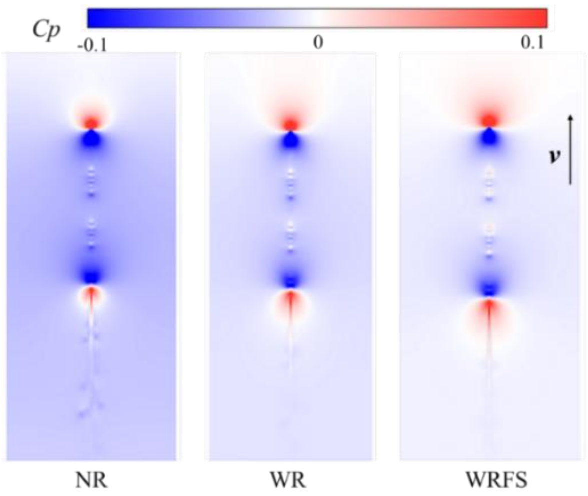

Fig. 11 Time averaged pressure contours on the ground

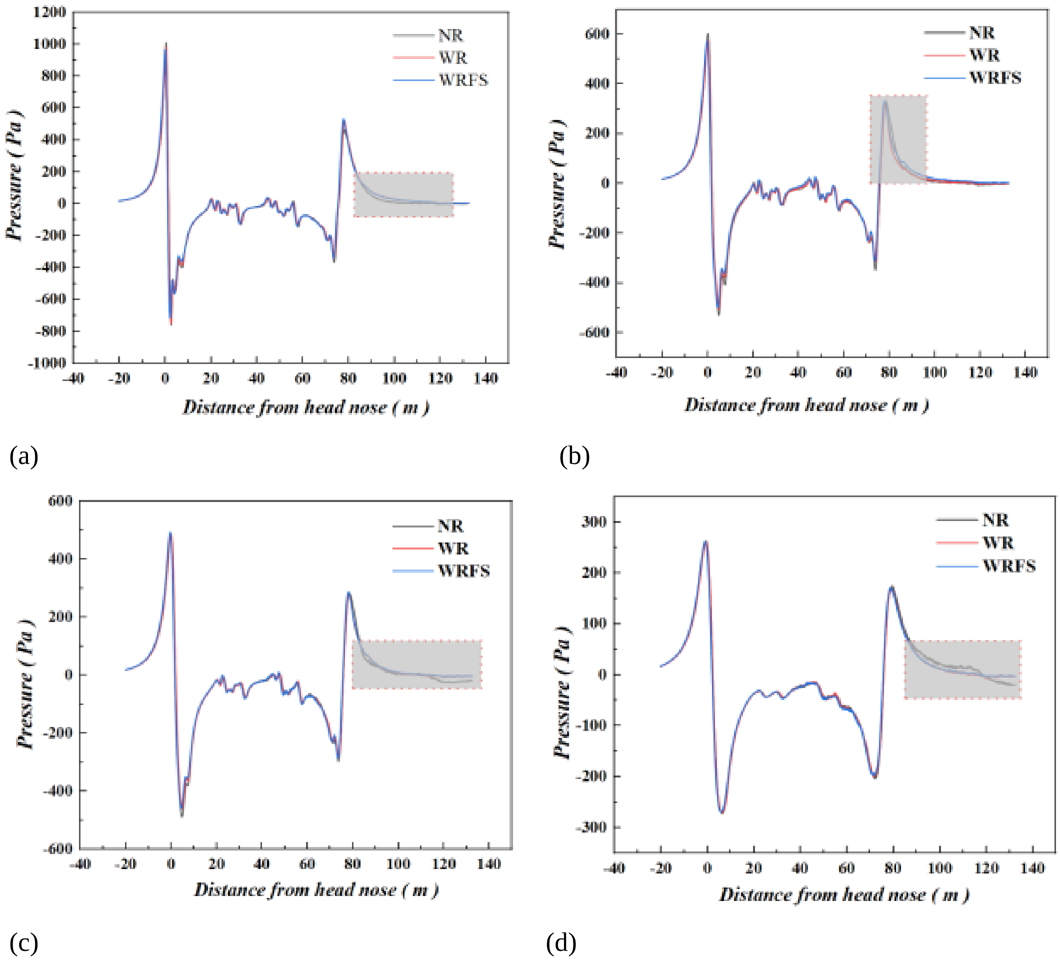

(a) (b) (c) (d)

Fig. 12 Pressure comparison of typical monitoring points: (a) M2; (b) M4; (c) M5; and (d) M7

Overall, the variations in lift and drag forces were not significant.

By comparing and analysing the pressures obtained from the monitoring points, several representative pressure comparison points were selected, as shown in Fig. 12. NR, WR, and WRFS all exhibited the same trend of pressure variation: at the front and rear of the train, there were two peaks corresponding to positive and negative pressures. With the increasing distance from the train, both the positive and negative pressure peaks gradually decreased. However, at monitoring points M2 and M4, the three models showed different positive pressure peaks at the front; specifically, for M2 they were 994Pa, 937Pa, and 925Pa, respectively, and for M4 they were 605Pa, 578Pa, and 576Pa, respectively. Additionally, the pressure at the rear of the train differed between NR and

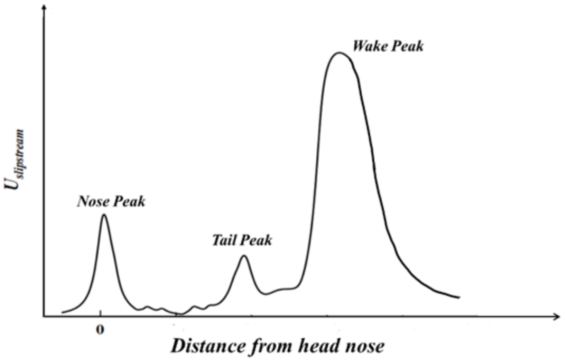

Fig. 13 Schematic diagram of high-speed train slipstream development

WR/WRFS. Overall, the pressure variations in WR and WRFS were largely consistent, while NR exhibited some differences from the other two configurations.

3.2 Slipstream Assessment

The focus of the present study was on the statistics of slipstream velocity at all monitoring points and the slipstream profile contour at the bottom of the train. The adoption of the sliding mesh technique brought the study closer to reality and allowed for more realistic slipstream results. Similar to previous sections, the time-domain data obtained from stationary monitoring points were transformed into the spatial domain. This involved converting the time-varying slipstream velocity into corresponding values for different parts. Given the substantial length of the wake and considering the primary research objectives and computational costs, the present study only involved investigating the development of the wake beyond the rear 56 meters of the train.

Generally, the slipstream of a train causes three slipstream velocity peaks, as shown in Fig. 13. One is at the front and one at the tail of the train, which are caused by the accelerating airflow. In the wake region of the train, a larger slipstream velocity peak develops due to coherent turbulence structures at different scales (Bell et al., 2014).

Figure 14 illustrates the distribution of slipstream velocity along the train body for all monitoring points M1-M11. For the three monitoring points M1-M3 at the bottom of the train, the slipstream velocity WR and WRFS remained consistent from 20 meters in front of the locomotive to 10 meters behind the tail. However, for NR, there were differences in slipstream velocity from the front to the rear, as shown in Fig. 14(a). At monitoring point M4 beside the track, Fig. 14(b) reveals significant differences in the peak values at the front and rear of the train, with NR consistently maintaining the highest slipstream velocity. In the WR and WRFS configurations, the presence of the track and fastening system blocked airflow in their vicinity, resulting in reduced velocity and

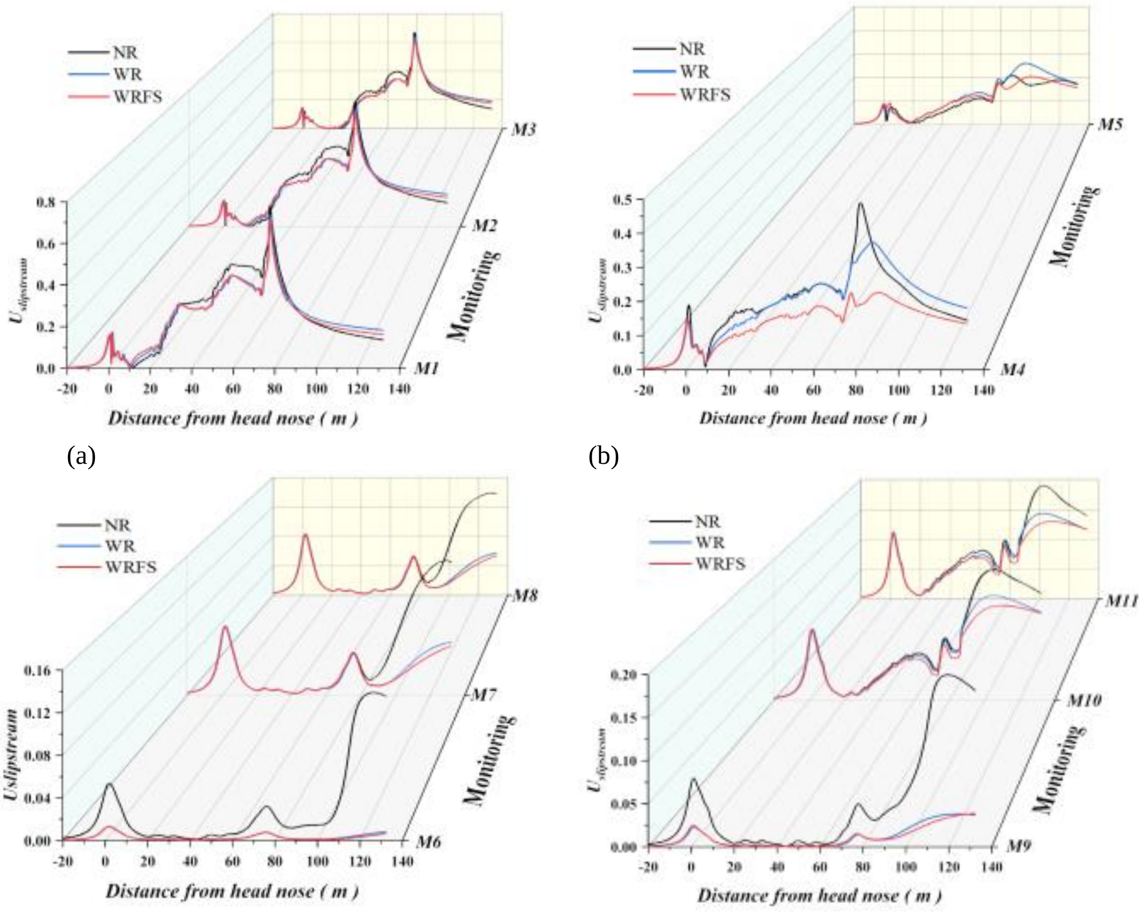

(a) (b)

(c) (d)

Fig. 14 Comparison of slipstream velocity at all monitoring positions: (a) M1-M3; (b) M4-M5; (c) M6-M8; and (d) M9-M11

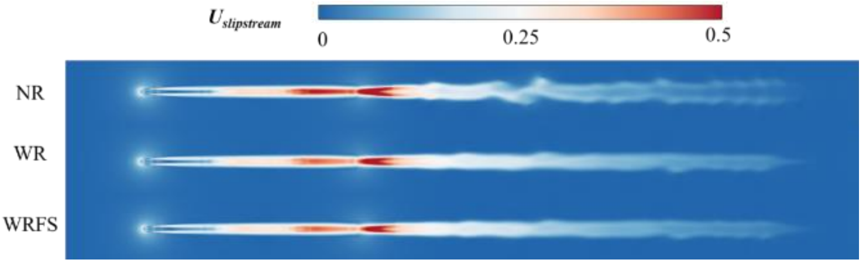

Fig. 15 Comparison of slipstream velocity ($U_{slipstream}$) at wheelset height level plane

Table 4 Comparison of nose peak slipstream velocity

Monitor point	**$U_{slipstream}$ Maximum**		
	NR	WR	WRFS
M1	0.163	0.159	0.158
M2	0.157	0.152	0.150
M3	0.150	0.145	0.142
M4	0.191	0.148	0.147
M5	0.081	0.089	0.090
M6	0.054	0.013	0.013
M7	0.080	0.080	0.079
M8	0.083	0.083	0.083
M9	0.078	0.023	0.025
M10	0.101	0.101	0.101
M11	0.113	0.111	0.111

a corresponding decrease in slipstream velocity, as illustrated in Fig. 14(b). Fig. 14(c) and Fig. 14(d) show the slipstream velocity at various distances and heights from the train. Monitoring points M6 and M9, positioned close to the ground and at a distance from the train, experienced substantial obstruction to lateral airflow from the train due to their low height and the presence of track and fastening systems. Hence, the slipstream velocities for WR and WRFS at these points were lower than those for NR. In addition, the monitoring points M7, M8, M10, and M11 were higher than the track, indicating a minimal effect on the slipstream velocity in the distance from the front end to the rear end. At the same time, the slipstream velocities of NR, WR and WRFS were highly consistent. The presence of tracks and the fastening system significantly affected the turbulent development of the wake, unlike NR, where there were no obstructions, allowing for the full development of turbulent phenomena at the rear, as depicted in Fig. 15. Consequently, the wake peak for NR was much higher than that for WR and WRFS.

Table 4 displays the comparison of the peak slipstream at the front of the car at all the monitoring points. M1-M4 consistently show that NR had the highest values, followed by WR and then WRFS. Moreover, the difference between NR and WR was significantly larger than that between WR and WRFS, with the disparity between WR and WRFS being minimal, such as 0.163-0.159-0.158. Monitoring point M5, located below the footstep, experienced a reduced weakening effect on slipstream velocity due to the presence of the track and fastening system. Therefore, the slipstream velocity gradually increased. The difference between the peaks of NR, WR and WRFS at the two monitoring points M6 and M9 has already been described. Monitoring points M7, M8, M10, and M11 were far from the train and track, and their peak values were essentially the same.

3.3 Wake Analysis

As discussed in this section, analysis of the wake was conducted from several aspects, including slipstream cross-sectional contours, the distribution of vorticity in different directions, the morphology of wake vortices, and the turbulent energy of the wake.

Figure 15 shows the slipstream velocity on the horizontal plane at the base wheels. It is evident that at the rear, the amplitude of the NR wake oscillations was greater. As the distance increased towards the rear, the wake split into two branches symmetric about the centreline, exhibiting a tendency to expand outward like rays. The shapes of the wake for WR and WRFS were highly consistent, as the track and fastening system hindered the development of the wake, resulting in a relatively narrow range of wake expansion.

Figure 16(a) shows the vortex distribution around the train along the streamwise direction (X+ direction). NR, WR and WRFS demonstrated consistent characteristic shapes. In the wake region, vortices predominantly rotated in the forward direction on the right side of the train, whereas on the left side, they rotated predominantly in the backward direction. In the middle of the wake, vortices of opposite directions alternated. However, the vorticity values along the forward direction for NR were notably higher than those for WR and WRFS, suggesting greater airflow rotation in this direction in the absence of the track. Similarly, in the region between the two bogies at the bottom of the train, the vorticity values for WR and WRFS were smaller due to the influence of tracks and the fastening system, as illustrated in Fig. 16(b).

The vortex distribution around the train along the spanwise direction (Y direction) is shown in Fig. 17. At the rear of the train, lateral vortices were symmetric about the centreline, and vortices in both directions appeared alternately, resembling branches of a tree. From NR to WR to WRFS, the amplitude of wake oscillation gradually decreased, but WR and WRFS were almost identical.

The vertical rotation of the air induced by the train was easily distinguishable and understandable, as shown in Fig. 18. From the passenger's perspective, the air on the right side of the train rotated clockwise, while the air on the left side rotated counterclockwise. As the boundary layer between the train and the air continued to develop

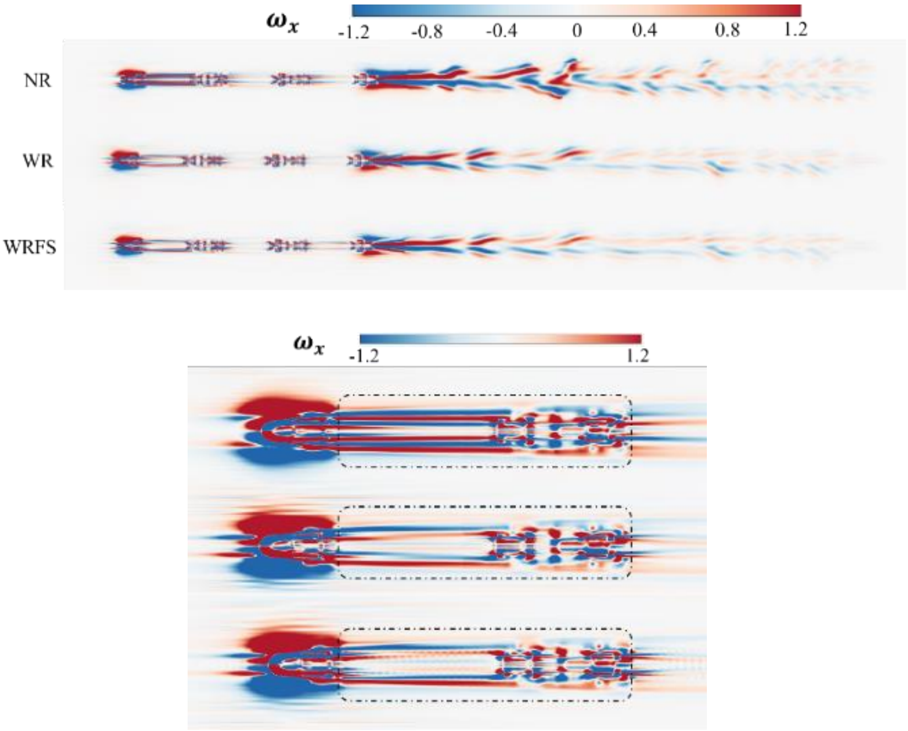

(a)

(b)

Fig. 16 Comparison of streamwise direction component of the vorticity in the plane of the rail: (a) Overall train; (b) Partial enlargement of the head car

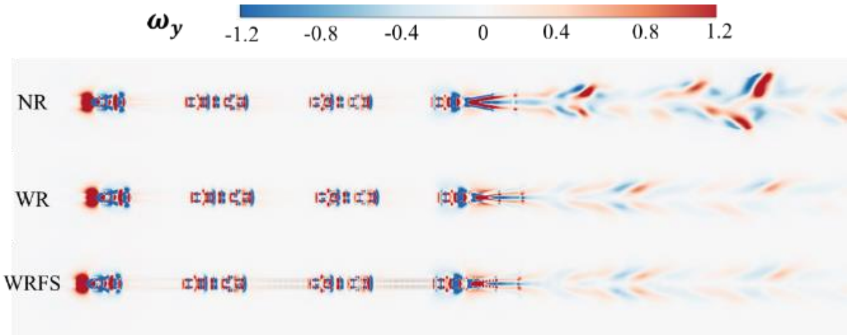

Fig. 17 Comparison of spanwise direction component of the vorticity in the plane of the rail

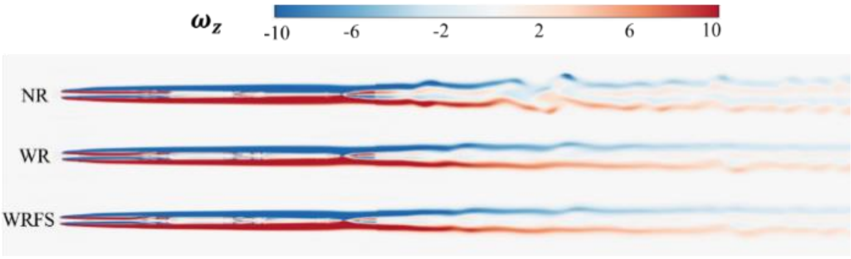

Fig. 18 Comparison of vertical direction component of vorticity in the plane of the rail

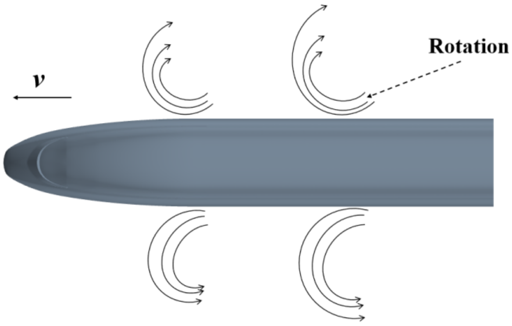

Fig. 19 Train-induced rotation of flow in the vertical direction

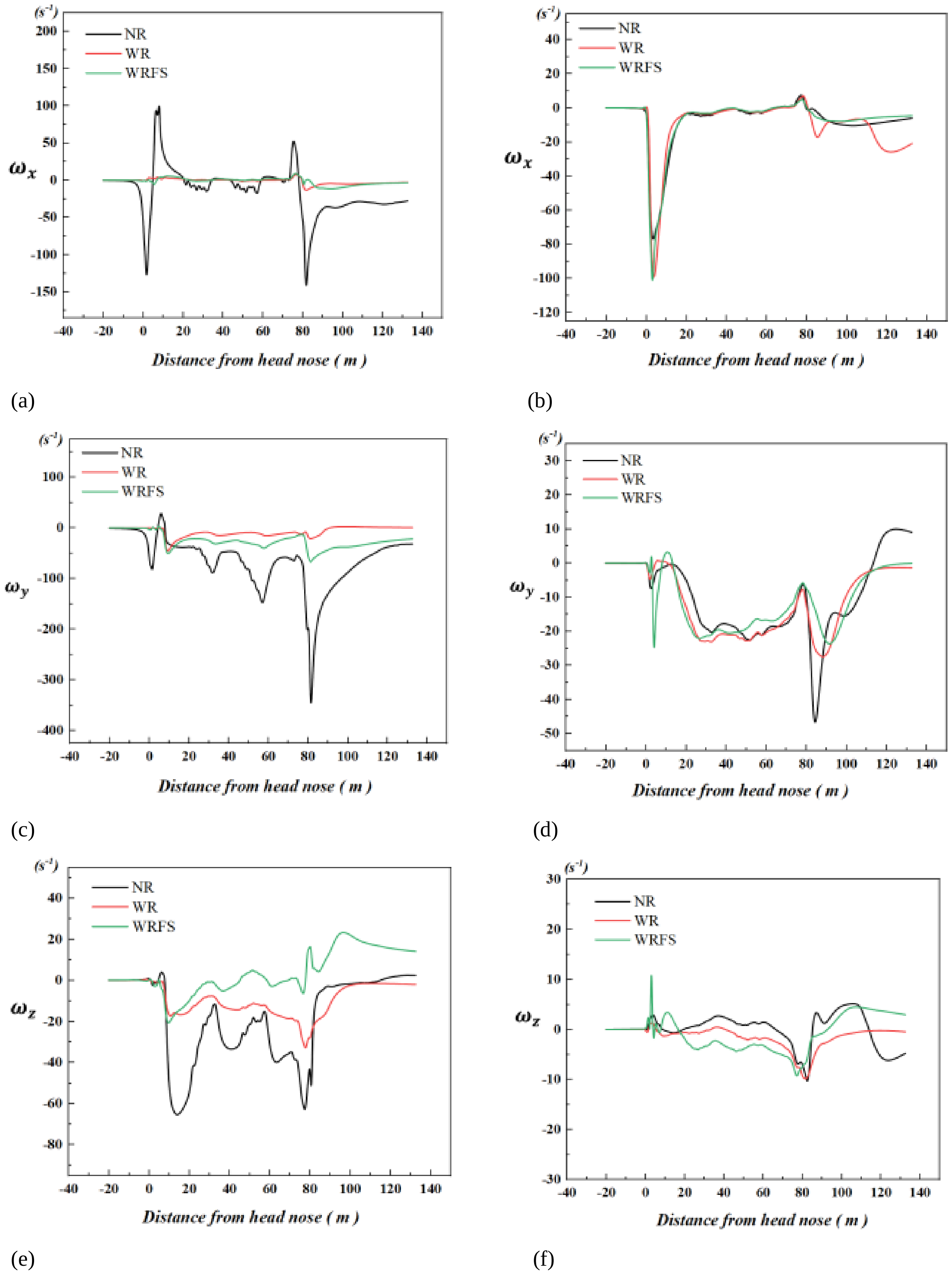

(a) (b)

(c) (d)

(e) (f)

Fig. 20 Comparison of three direction components of vorticity: (a) (c) (e) M4; and (b) (d) (f) M5

and thicken, the rotation of the airflow intensified, as illustrated in Fig. 19. Figure 20(e) displays the vorticity in the vertical direction along the line at the location of monitoring point 4. It was apparent from the plot depicting the vortex change in the figure that the head train exhibited increasing vorticity from front to back, indicating heightened rotation of the airflow in that direction. Between the train nose and tail, the vertical vortex values of NR, WR and WRFS were consistent. At the train rear, due to the limiting effect of the tracks and fastening system, the spatial extent of vortex values in this direction for WR and WRFS was markedly less than for NR.

Monitoring point M4 was positioned beside the rail track, while monitoring point M5 was situated at the footstep next to the track. These two locations were the most severely affected by the rail track and fastening system. To obtain a clearer understanding of the flow field near the bottom of the train track, changes in vorticity in

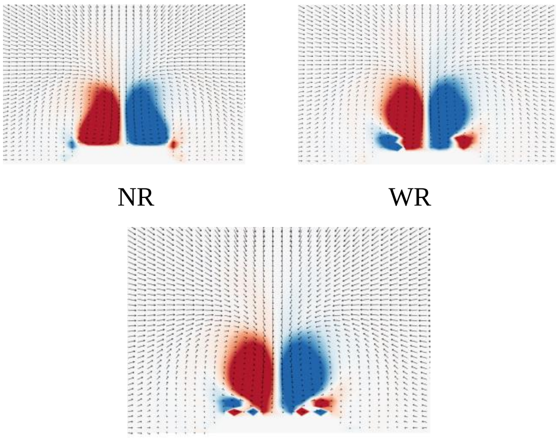
NR WR

WRFS

Fig. 21 Comparison of velocity vector and streamwise direction component of vorticity at 2m from the tail of the train

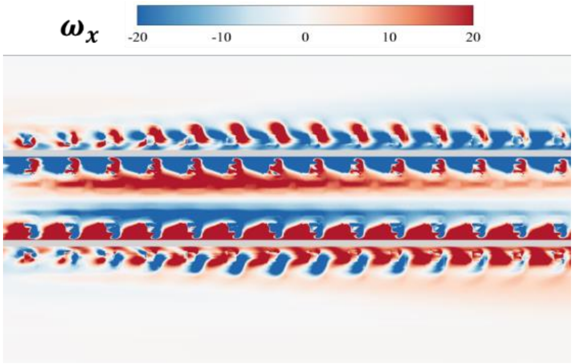

Fig. 22 Vortex detail near fastener system in WRFS

different directions at monitoring points M4 and M5 were monitored, as depicted in Fig. 20(a)-(f). For monitoring point M4, the vorticity in three directions exhibited significant peaks at the front and rear for NR, while the changes for WR and WRFS were gradual. This was because monitoring point M4 was close to the tracks and fastening system, impeding the development of turbulence. Monitoring point M5 was situated below the footstep, indicating that the track and fastening system had a pronounced impact on lateral vortices, whereas the impact on the other two directions was smaller. This aligns with the peak observed exclusively for NR in Fig. 20(d). Overall, WR and WRFS also showed some differences, but these were minor fluctuations within a narrow range, lacking the extensive turbulence development observed for NR.

Figure 21 overlays the velocity vectors and streamwise vorticity contours at the rear. The bilateral symmetry of the train wake along the X-direction is distinctly exhibited. Two contra-rotating vortices resembling a dual-helix structure propagated rearwards. Comparing NR and WR, it is evident that the track exerted a compressive effect on the near-ground airflow, significantly impeding the outward expansion of the airflow. For NR, the wake spread wider near the top than the bottom, whereas the opposite trend occurred for WR.

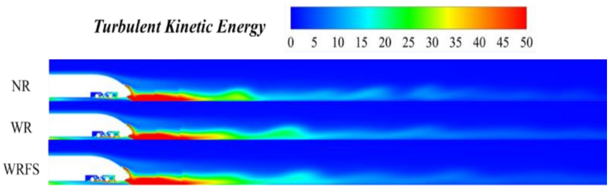

Fig. 23 Comparison of turbulent kinetic energy in the near wake

Meanwhile, in the ballastless track, the step ground can induce airflow separation at the footsteps, resulting in the formation of secondary vortices. The presence of the track further facilitated the formation of these secondary vortices. Regarding WRFS, the vortex shapes were largely consistent with WR, although the dispersion of ground-level airflow was more tightly constrained. Further, the complex structure of the fastening system can lead to the appearance of some smaller vortices in its vicinity, as shown in Fig. 22. The major vortices and those near the fastening system on both sides followed a consistent rotation pattern, with external airflows curling inward toward the centreline. As the train moved rapidly forward, a negative pressure zone formed behind it, causing the air on both sides to quickly converge towards the centre of the track, explaining the distribution of the vortices in this manner.

Figure 23 illustrates the comparison of turbulence kinetic energy in the wake flow. Evidently, in the region near the rear, from NR to WR to WRFS, the dissipation of turbulence kinetic energy slowed down. This indicates that tracks and the fastening system disrupted the flow field structure of the wake, intensifying the turbulence disorder and leading to an increase in turbulence kinetic energy near the rear of the train. Further downstream, at a sufficient distance from the tail, the turbulent kinetic energy remained approximately identical for all cases, gradually dissipating over time.

4. CONCLUSION

Through investigating the impacts of the rail track and fastening system on the aerodynamic performance, slipstream and wake flows of high-speed trains, the following conclusions were drawn:

(1) The rail tracks and fastening system had certain influences on the train aerodynamics. The drag force coefficients of NR, WR and WRFS were 0.2730, 0.2750 and 0.2786, respectively, increased by 0.73% and 2.05%, respectively. Simultaneously, the lift force coefficients for each car were also affected. The pressure changes at monitoring points for WR and WRFS were generally consistent, while NR showed some differences from the other two.

(2) The rail track and fastening system barely affected the slipstream velocity away from the ground around the train. The slipstream underneath, particularly adjacent to the tracks and fastening system, experienced noticeable changes. Additionally, the train exerted the maximum slipstream influence on the far-field

ground in NR. WR and WRFS showed minimal differences in monitored slipstream velocity.

(3) The rail track and fastening system had certain mitigation effects on the three components of vorticity surrounding the train. The wake flows developed most fully for NR, while the constrained wake developments gradually strengthened for WR and WRFS. The tracks and fastening system modified the dual-helix wake vortex shapes and intensified secondary vortices near the track. Moreover, the near-wake turbulent kinetic energy grew progressively from NR to WR to WRFS.

In summary, the absence of a track model significantly impacted the aerodynamic performance, slipstream, and wake of high-speed trains. Establishing a track model that includes a fastening system can capture more flow field details, yielding results closer to reality. However, the differences between WR and WRFS are not substantial across various aspects. Notably, the fastening system led to a significant increase in the number of grids, resulting in higher computational costs and time. If conditions allow, the use of WRFS is naturally preferred. Yet, in many cases, balancing accuracy and cost-effectiveness, employing a model that includes only a track (WR) is sufficient for calculations.

ACKNOWLEDGEMENTS

The author(s) disclosed receipt of the following financial support for the research, authorship and/or publication of this article: This work was funded by The National Natural Science Foundation of China (Grant No. 12172308).

CONFLICT OF INTEREST

No potential conflict of interest was reported by the authors.

AUTHORS CONTRIBUTION

Yuzhe Ma: Writing – Original draft, Data curation, Methodology, Validation, Visualization. **Jiawei Shi:** Conceptualization, Writing - Review & Editing. **Yangyang Cao:** Software, Writing - Review & Editing. **Jiye Zhang:** Writing - Review & Editing, Funding acquisition.

REFERENCES

Baker, C. (2010). The flow around high speed trains. *Journal of Wind Engineering and Industrial Aerodynamics,* *98*(6-7), 277-298. https://doi:10.1016/j.jweia.2009.11.002

Bell, J. R., Burton, D., Thompson, M. C., A. H. Herbst, & J. Sheridan (2015). Moving model analysis of the slipstream and wake of a high-speed train. *Journal of Wind Engineering and Industrial Aerodynamics, 136*, 127-137. https://doi:10.1016/j.jweia.2014.09.007

Bell, J. R., Burton, D., Thompson, M., A. H. Herbst, & J. Sheridan (2014). Wind tunnel analysis of the slipstream and wake of a high-speed train. *Journal of Wind Engineering and Industrial Aerodynamics, 134*, 122-138. https://doi:10.1016/j.jweia.2014.09.004

CEN European Standard (2009). Railway Applications—Aerodynamics—Part 4: Requirements and Test Procedures for Aerodynamics on Open Track, CEN EN 14067-4.

CEN European Standard (2010). Railway Applications—Aerodynamics—Part 6: Requirements and Test Procedures for Cross Wind Assessment, CEN EN 14067-6.

CEN European Standard (2013). Railway Applications—Aerodynamics—Part 4: Requirements and Test Procedures for Aerodynamics on Open Track, CEN EN14067-4.

Cheli, F., Corradi, R., Rocchi, D., Tomasini.G, & Maestrini. E (2010). Wind tunnel tests on train scale models to investigate the effect of infrastructure scenario. *Journal of Wind Engineering and Industrial Aerodynamics*, *98*(6-7), 353-362. https://doi:10.1016/j.jweia.2010.01.001

Chu, C. R., Chien, S. Y., Wang, C. Y., & Wu, T. R. (2014). Numerical simulation of two trains intersecting in a tunnel. *Tunnelling and Underground Space Technology*, *42*, 161-174. https://doi:10.1016/j.tust.2014.02.013

Fluent Inc. (2015). Fluent Theory Guide.

Jönsson, M., Wagner, C., & Loose, S. (2014). Particle image velocimetry of the underfloor flow for generic high-speed train models in a water towing tank. *Proceedings of the Institution of Mechanical Engineers, Part F: Journal of Rail and Rapid Transit*, *228*(2), 194-209. https://doi:10.1177/0954409712470607

Niu, J., Wang, Y., Liu, F., & Li, R. (2021). Numerical study on comparison of detailed flow field and aerodynamic performance of bogies of stationary train and moving train. *Vehicle System Dynamics*, *59*(12): 1844-1866. https://doi:10.1080/00423114.2020.1794015

Paz, C., Suárez, E., & Gil, C. (2017). Numerical methodology for evaluating the effect of sleepers in the underbody flow of a high-speed train. *Journal of Wind Engineering and Industrial Aerodynamics, 167*: 140-147. https://doi:10.1016/j.jweia.2017.04.017

Raghunathan, R. S., Kim, H, D., & Setoguchi, T. (2002). Aerodynamics of high-speed railway train. *Progress in Aerospace sciences*, *38*(6-7), 469-514. https://doi:10.1016/S0376-0421(02)00029-5

Soper, D., Baker, C., Jackson, A., Milne, D. R., Le Pen, L., Watson, G., & Powrie, W. (2017). Full scale measurements of train underbody flows and track forces. *Journal of Wind Engineering and Industrial*

Aerodynamics, *169*, 251-264. https://doi:10.1016/j.jweia.2017.07.023

Sun, Z., Zhang, Y., Guo, D., Yang, G., & Liu, Y. (2014). Research on running stability of CRH3 high speed trains passing by each other. *Engineering Applications of Computational Fluid Mechanics*, *8*(1), 140-157. https://doi:10.1080/19942060.2014.11015504

Tian, H. Q. (2019). Review of research on high-speed railway aerodynamics in China. *Transportation Safety and Environment*, *1*(1). https://doi:10.1093/tse/tdz014

Wang, J., Wang, T., Yang, M., Qian, B., Zhang, L., Tian, X., & Shi, F. (2022). Research on the influence of different heating zone lengths on pressure waves and a newly designed method of pressure wave mitigation in railway tunnels. *Tunnelling and Underground Space Technology*, *122*, 104379. https://doi:10.1016/j.tust.2022.104379

Wang, S., Bell, J. R., Burton, D., Herbst, A. H., Sheridan, J., & Thompson, M. C. (2017). The performance of different turbulence models (URANS, SAS and DES) for predicting high-speed train slipstream. *Journal of Wind Engineering and Industrial Aerodynamics*, *165*, 46-57. https://doi:10.1016/j.jweia.2017.03.001

Wang, S., Burton, D., Herbst, A. H., Sheridan, J., & Thompson, M. C. (2020). The impact of rails on high-speed train slipstream and wake. *Journal of Wind Engineering and Industrial Aerodynamics*, *198*, 104114. https://doi:10.1016/j.jweia.2020.104114

Wang, S., Burton, D., Herbst, A., Sheridan, J., & Thompson, M. C. (2018). The effect of bogies on high-speed train slipstream and wake. *Journal of Fluids and Structures*, *83*, 471-489. https://doi:10.1016/j.jfluidstructs.2018.03.013

Wang, Y., Wang, T., Jiang, C., Wu, Y., Zhao, C., Shi, F., & Tian, X. (2023). Numerical study on slipstream-induced snow drifting and accumulation in the bogie region of a high-speed train passing the snowy ballast bed. *Journal of Wind Engineering and Industrial Aerodynamics*, *232*, 105269. https://doi:10.1016/j.jweia.2022.105269

Xia, C., Shan, X., & Yang, Z. (2017). Comparison of different ground simulation systems on the flow around a high-speed train. *Proceedings of the Institution of Mechanical Engineers, Part F: Journal of Rail and Rapid Transit*, *231*(2), 135-147. https://doi:10.1177/0954409715626191